Relativistic and nondipole effects in multiphoton ionization of hydrogen by a high-intensity x-ray laser pulse

Johanne Elise Vembe ©,* Esther A. B. Johnsen ©, and Morten Førre ©†
Department of Physics and Technology, University of Bergen, 5020 Bergen, Norway

In the theory of multiphoton ionization, the effects of relativity and spatial dependence in the laser field are typically neglected for the sake of computational feasibility, as well as being too small to measure. As advances in high-intensity, short-wavelength lasers are developed, ultimately it becomes necessary to investigate the impact of relativistic and/or beyond-dipole (nondipole) corrections, as they are no longer small enough to neglect. Using an *ab initio* approach and the time-dependent Dirac equation to simulating the ionization process in an exact nondipole treatment, we study the high-intensity multiphoton ionization of hydrogen by a short x-ray laser pulse in the relativistic regime, yielding the kinetic-energy spectrum of the photoelectron, and observe a shift in the energy of the emitted electron as induced by relativistic and nondipole effects. Overall, relativistic effects are seen to give rise to a positive energy shift (blueshift), while nondipole effects cause a corresponding negative shift (redshift), and in aggregate the relativistic and nondipole ionization result in a tiny redshift. Considering only photoelectrons that are emitted along the laser polarization direction, the blueshift is recovered, and the shift may be explained in terms of the relativistic mass shift of the electron in the oscillating field.

I. INTRODUCTION

When studying the interaction of electromagnetic radiation with matter, relativistic effects may be ignored provided the intensity of the incident radiation is so small that the dynamics is adequately described by nonrelativistic equations of motion. Rapid development in the field of high-intensity lasers may soon necessitate that these effects are addressed, however. As the intensity increases, at some point the non-relativisitic approximation will break down, which demands modeling the phenomena in a relativistic treatment [1–12]. Entering the relativistic regime comes with the additional burden that the widely used dipole approximation is no longer valid, i.e., the spatial dependency of the incident laser beam cannot be neglected in the theoretical analysis, and the laser's magnetic-field component must be accounted for. There has been a growing interest in studying strong-field ionization of atoms and molecules beyond the dipole approximation, both theoretically [13–22] and experimentally [23–32].

The dipole approximation is generally not valid for intense x-ray laser fields [17,33]. It is then necessary to address the spatial dependency to accurately model the now-relevant beyond dipole effects such as the radiation pressure [34]. Furthermore, the nonrelativistic approximation ultimately breaks down as the radiation field grows high enough [9]. From the point of view of theoretical modeling, including both relativistic as well as beyond-dipole (nondipole) effects carries a numerical cost. When working in a nonrelativistic framework the dynamics of an electron can sufficiently be described by the Schrödinger equation, but in a fully relativistic treatment it is necessary to use the Dirac equation, which has several computational hurdles to overcome in comparison. The same applies to a nondipole treatment of the laser field, as the nondipole effects demand a quadratic increase in the size of the basis in which the electron's wave function is expressed. Several attempts for solving the time-dependent Dirac equation in full dimensionality with space-time varying electromagnetic radiation have been pursued [6,7,29,35–39].

Recently, the multiphoton ionization of the hydrogen $1s$ electron by an intense 1.36 keV x-ray laser pulse of intensity $\sim 10^{22}$ W/cm^2 was studied theoretically [9,40], taking into account both beyond-dipole and relativistic effects. In these studies the role of the nondipole field was modeled in an approximate fashion, writing out the laser vector potential in terms of a Maclaurin series expansion and keeping only the leading-order term beyond the dipole approximation. Furthermore, most calculations were executed within the context of a semirelativistic time-dependent Schrödinger equation formulation [41,42], i.e., the fully relativistic time-dependent Dirac equation was only solved imposing additional constraints on the field in terms of the so-called long-wavelength approximation [43]. Notwithstanding, the studies revealed that including both relativistic as well as nondipole effects is crucial for a proper description of the laser-matter interaction. It was also shown that nondipole effects generally lead to a redshift of the kinetic-energy spectrum of the emitted photoelectron, while relativistic effects result in a corresponding blueshift, of which both shifts appear to be of similar size. The relativistic blueshift was very recently reproduced in an independent study solving the time-dependent Klein-Gordon equation for a spinless particle [44], assuming the dipole approximation. Further, in the same study the corresponding nondipole redshift was obtained solving the time-dependent Schrödinger equation (TDSE) beyond the dipole approximation.

*Johanne.Vembe@uib.no
†Morten.Forre@uib.no

In this work, we go one step further and solve for the fully relativistic and nondipole multiphoton ionization dynamics of the hydrogenic atom exposed to the ultrashort 1.36 keV x-ray pulse, maintaining the exact spatial dependence of the laser field. To this end, the time-dependent Dirac equation (TDDE) is discretized and solved essentially without any approximations in a very large set of basis functions, aiming at minimizing any numerical and truncation errors. We then perform a systematic study of the impact of both relativistic and nondipole effects in the underlying multiphoton ionization, with emphasis on relativistic blue- and nondipole redshifting of the resulting electron energy distributions. Further, we investigate the relative magnitudes of these two effects and how they relate to the intensity of the laser pulse, both separately and when the two effects are accounted for at the same time. It is found that relativistic and beyond-dipole effects both become important as the laser peak intensity exceeds 10^{20} W/cm^2. Of concern here is the fact that the resulting relativistic and nondipole shifts are opposites, but even more importantly that they are of similar size. This means that they must both be treated on an equal footing when it comes to energy observables, which indeed is a surprising result given that relativistic effects are not expected to be important at these (low) laser intensities in the x-ray regime [45,46]. A distinct possibility to look out for here is that nondipole and relativistic effects interact in some way, and so cannot simply be handled separately. State-of-the-art calculations with both the TDDE and the TDSE, respectively, and subsequent detailed analysis of the kinetic energy of the outgoing photoelectron, merely demonstrate that relativistic and nondipole effects, when considered altogether, ultimately lead to a (tiny) redshift of the (total) differential photoelectron energy spectrum. Presuming that electrons that are emitted along the laser polarization axis are most influenced by relativity and least by nondipole effects, these were analyzed separately, and the relativistic blueshift was retrieved. Finally, interpreting the results in terms of the relativistic mass increase of the electron in the laser field, we derived a simple scaling law for the size of this blueshift.

Atomic units (a.u.) are used where stated explicitly.

II. THEORY AND METHODS

We here simply model the hydrogen atom quantum mechanically in terms of an electron of mass m and charge $-e$ moving in a Coulomb potential, effectively treating the nucleus as a static classical particle. The potential energy associated with the electron's motion in the potential well is given by $V(r) = -\frac{e^2}{4\pi\varepsilon_0 r}$, with e being the elementary charge, ε_0 the permittivity of free space, and r the distance of the electron from the nucleus. We further introduce the interaction with an external electromagnetic field, i.e., a laser pulse, as defined by the vector potential $A(r, t)$, and which is also taken to be a classical one, as its intensity is assumed to be too high to treat photons as quantized particles. The time evolution of the electron wave function $\psi(r, t)$ is generally governed by the equation of motion,

$$i\hbar \frac{\partial}{\partial t}\psi = H\psi, \qquad (1)$$

where $\hbar$ is the reduced Planck constant and H is the system Hamiltonian.

We use three different model Hamiltonians for the different cases to be studied here. First, in the purely nonrelativistic limit the standard minimal-coupling Schrödinger Hamiltonian is applied,

$$H = \frac{1}{2m}[p + eA(r, t)]^2 + V(r). \qquad (2)$$

Here, p is the momentum operator, and we have used the minimal coupling prescription $p \rightarrow p + eA(r, t)$ to impose interaction with the external field. Then, in the context of a fully relativistic model, we instead make use of the Dirac formulation of the light-matter interaction,

$$H = \beta mc^2 + I_4 V(r) + c \sum_{i=1}^{3} \alpha_i [p_i + eA_i(r, t)], \qquad (3)$$

where $i = 1, 2, 3$ refers to the x, y, and z components, respectively, c is the speed of light, I_4 is the 4×4 identity matrix, and β and α_i ($i = 1, 2, 3$) are the Dirac matrices, given in block matrix form by

$$\beta = \begin{pmatrix} I_2 & 0 \\ 0 & -I_2 \end{pmatrix}, \quad \alpha_i = \begin{pmatrix} 0 & \sigma_i \\ -\sigma_i & 0 \end{pmatrix}. \qquad (4)$$

Here, σ_i are the Pauli matrices and I_2 is the 2×2 identity matrix.

Finally, in the third approach a semirelativistic Schrödinger light-matter interaction formulation is considered. This scheme is computationally very advantageous compared to the Dirac approach, and may be a useful tool in exploring the underlying relativistic ionization mechanisms at play. For this minimal relativistic approach to the Schrödinger equation, which includes relativistic corrections to the kinetic energy but neglects any spin degrees of freedom, the corresponding semirelativistic Hamiltonian for the electron is given by

$$\begin{aligned} H &= \sqrt{m^2c^4 + (p + eA)^2 c^2} - mc^2 + V \\ &= \frac{(p + eA)^2}{2m} - \frac{(p + eA)^4}{8m^3c^2} + \cdots + V \\ &= \frac{p^2}{2m} + V + \frac{e}{m}A \cdot p + \frac{e^2}{2m}A^2 - \frac{p^4}{8m^3c^2} - \frac{e^4}{8m^3c^2}A^4 \\ &\quad - \frac{e}{4m^3c^2}\{A \cdot p, p^2\} - \frac{e^2}{8m^3c^2}\{A^2, p^2\} \\ &\quad - \frac{e^3}{2m^3c^2}A^2 A \cdot p - \frac{e^2}{2m^3c^2}(A \cdot p)^2 + \cdots, \end{aligned} \qquad (5)$$

where curly brackets {} indicate an anticommutator and where the Coulomb gauge condition $\nabla \cdot A = 0$ is assumed.

Solving the TDSE with Eq. (5) is expected to deliver results in accordance with the exact solution to the Klein-Gordon equation, provided the series expansion of the Hamiltonian converges. Note, however, that the equation of motion does not have a covariant form in the semirelativistic representation, so care has to be taken when drawing conclusions from the results. Nevertheless, the validity of the Maclaurin series expansion is determined by its radius of convergence. Here the expansion parameter is $(p + eA)^2/m^2c^2$ and, as such, the

condition of convergence of the series becomes

$$\frac{|\boldsymbol{p} + e\boldsymbol{A}|^2}{m^2 c^2} < 1. \qquad (6)$$

To guarantee validity, this constraint must be met at all times throughout the laser-matter interaction. Notice that the convergence properties of the series will generally not be altered by introducing a gauge transformation to the fields, i.e., letting $\boldsymbol{A} \to \boldsymbol{A} + \nabla f$ in Eq. (5), with $f(\boldsymbol{r}, t)$ being an arbitrary differentiable function of $\boldsymbol{r}$ and t, as the role of the (canonical) momentum $\boldsymbol{p}$ will change accordingly. In this work, all calculations are executed within the minimal coupling scheme, which in the dipole and nonrelativistic limit is commonly referred to as the *velocity gauge*. In this representation, the momentum becomes approximately a constant of motion in the (intense) laser field, and therefore the semirelativistic approach is justified if the condition

$$\frac{e^2 A^2}{m^2 c^2} < 1 \qquad (7)$$

is fulfilled. If one instead were to solve the equation of motion in the so-called *length gauge* representation, simply choosing $f(\boldsymbol{r}, t) = -\boldsymbol{A} \cdot \boldsymbol{r}$ and again assuming the dipole approximation, then $\boldsymbol{p}$ plays the role of the real physical momentum, and the convergence criteria would have become $p^2/(m^2 c^2) < 1$ instead.

Now, considering only transient (time-dependent) relativistic effects and ignoring any relativistic structure effects, such as the (time-independent) relativistic correction to the kinetic energy, i.e., the p^4 term, as well as keeping only the leading-order dynamical relativistic corrections induced by the (dipole) laser field, the semirelativistic Hamiltonian further simplifies to

$$
\begin{aligned}
H \simeq \ &\frac{p^2}{2m} + V + \frac{e}{m}\boldsymbol{A}(\boldsymbol{r}, t) \cdot \boldsymbol{p} + \frac{e^2}{2m}A^2(\boldsymbol{r}, t) - \frac{e^4}{8m^3 c^2}A_0^4(t) \\
&- \frac{e}{2m^3 c^2} p^2 \boldsymbol{A}_0(t) \cdot \boldsymbol{p} - \frac{e^2}{4m^3 c^2} p^2 A_0^2(t) \\
&- \frac{e^3}{2m^3 c^2} A^2 \boldsymbol{A}_0(t) \cdot \boldsymbol{p} - \frac{e^2}{2m^3 c^2}[\boldsymbol{A}_0(t) \cdot \boldsymbol{p}]^2,
\end{aligned} \qquad (8)
$$

where the vector potentials $\boldsymbol{A}$ and $\boldsymbol{A}_0$ are further specified in Eqs. (9) and (10) below, and representing the full beyond-dipole (nondipole) and dipole fields, respectively. Note here that the full spatial dependence of the vector potential is still accounted for in the nondipole interaction terms in Eq. (8), while only the dipole component of the field is considered in the relativistic corrections.

In order to solve for the time evolution of the system in the semirelativistic and nonrelativistic limits, respectively, the time-dependent Schrödinger equation (TDSE) in Eq. (1) with the Hamiltonians (2) and (8) is discretized using spherical coordinates and with the wave function ψ expanded in a finite set of bound and unbound eigenstates of the field-free atomic Hamiltonian, following the procedures described in Refs. [9,33]. Details of the fully relativistic calculations with the time-dependent Dirac equation (TDDE) are given in Sec. II B.
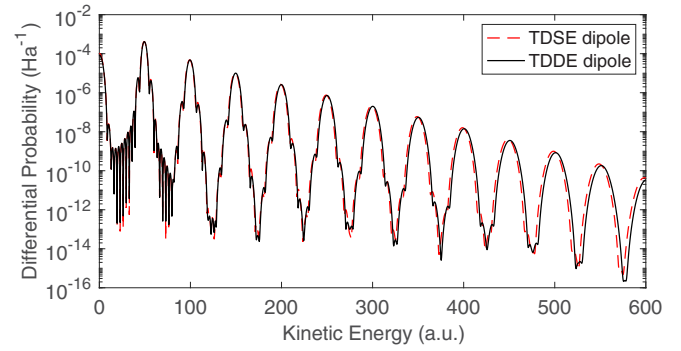

FIG. 1. Differential photoelectron kinetic-energy spectrum of the emitted photoelectron, as obtained from Eq. (36), and plotted as a function of the kinetic energy (in atomic units) of the emitted photoelectron. Note that the abbreviation Ha on the y axis refers to Hartree, the atomic unit of energy. The distribution is obtained for the dipole field defined in Eq. (10), with the electric-field amplitude $E_0 = 600$ a.u., angular frequency $\omega = 50$ a.u., and for a 15-cycle laser pulse. The red (dashed line) and black spectra are obtained from solving the nonrelativistic time-dependent Schrödinger equation (TDSE) and the relativistic time-dependent Dirac equation (TDDE), respectively, in the dipole approximation. In total twelve multiphoton peaks are depicted in the spectra, corresponding to the net absorption of 1–12 photons from the field. The relativistic spectrum is shifted to higher energies with respect to the corresponding nonrelativistic spectrum, manifesting the relativistic blueshift, which arise when relativistic corrections are accounted for in the system.

The laser pulse is modeled in terms of the vector potential $\boldsymbol{A}$ as

$$\boldsymbol{A}(\boldsymbol{r}, t) = \frac{E_0}{\omega} \sin^2\left(\frac{\pi t}{T} - \frac{\pi}{cT}\hat{\boldsymbol{k}} \cdot \boldsymbol{r}\right) \sin\left(\omega t - \boldsymbol{k} \cdot \boldsymbol{r}\right)\hat{\boldsymbol{u}}_p, \quad (9)$$

where $\boldsymbol{k} = \frac{\omega}{c}\hat{\boldsymbol{k}}$ is the wave vector defining the laser propagation direction, $\hat{\boldsymbol{u}}_p$ is the polarization vector, E_0 is the electric-field strength at peak intensity, and ω is the central angular frequency of the laser field. The pulse duration T is set to achieve a certain number of cycles—in the scope of this work 15 cycles. Note that the vector potential includes the full spatial dependence of the field and, as such, it needs special handling due to our choice of spherical coordinates for expressing the interaction Hamiltonians. This issue is elaborated on in Sec. II A.

With all model ingredients assembled, the numerical simulations performed serve to retrieve the wave function Ψ_t, which is the state of the system after a single pulse of the laser has interacted with the hydrogen atom. This is done by approximating the time evolution of the system, Eq. (1), in a finite number of time steps; see Sec. II C. Then, we may obtain the differential probability spectrum $\frac{dP}{dE}$ by taking the inner products of Ψ_t with the eigenstates of the Hamiltonian, as discussed in Sec. III.

Figure 1 shows an example of two differential photoelectron energy spectra obtained using the nonrelativistic Schrödinger and relativistic Dirac formulations, respectively, merely demonstrating the phenomenon we are looking for: the multiphoton ionization resonances are located at slightly different positions in energy depending on which framework the spectrum has been computed from. In this example the

hydrogen 1s electron has been exposed to a 15-cycle laser pulse of angular frequency $\omega = 50$ a.u. and peak electric field strength $E_0 = 600$ a.u. The figure reveals a general feature of the multiphoton ionization dynamics in that the relativistic spectrum becomes shifted to higher energies with respect to its nonrelativistic counterpart, resulting in a relativistic blueshift. Measuring this shift in the spectra is our primary goal. Although, for the sake of simplicity, the dipole approximation was assumed here, we shall see shortly that the relativistic blueshift is a general characteristic of the multiphoton ionization process at high laser intensities.

A. Laser pulse potential

As we model our system in spherical coordinates, it is advantageous for our external vector potential to be modeled in spherical coordinates as well. Unfortunately, as Eq. (9) shows, the laser pulse is evidently not spherically symmetric. Both the $\hat{\boldsymbol{k}}$ and polarization vector $\hat{\boldsymbol{u}}_p$ are assumed to lie in a Cartesian coordinate system, leading to difficulties in expressing the potential spherically which will be addressed shortly. A simple and often very effective way around part of this problem is the dipole approximation, in which we neglect spatial dependence entirely, resulting in

$$\boldsymbol{A}_0(t) = \frac{E_0}{\omega} \sin^2\left(\frac{\pi t}{T}\right) \sin(\omega t) \hat{\boldsymbol{u}}_p. \tag{10}$$

While this is very often sufficient, the goal of this work depends on including the full spatial dependency of the problem. Following the lines of [33], we reformulate the nondipole vector potential in spherical coordinates, first by using trigonometric identities to separate time- and space-dependent components of the potential, then by using the Bessel function expansion of plane waves. In this way, we arrive at the following form for the vector potential:

$$\boldsymbol{A}(\boldsymbol{r}, t) = \hat{\boldsymbol{u}}_p \sum_{\alpha=1}^{6} f_\alpha(t) \sum_{lm} g_{\alpha,l}(r) Y_{lm}^*(\hat{\boldsymbol{k}}) Y_{lm}(\hat{\boldsymbol{r}}). \tag{11}$$

Here, Y_{lm} are spherical harmonics and the summation coefficient α arises from the aforementioned separation by trigonometric identities. We have introduced time-dependent functions $f_\alpha(t)$ and radial functions $g_{\alpha,l}(r)$, with the functions f_α defined as

$$f_\alpha(t) = \begin{cases} D_\alpha \sin(C_\alpha t), & \alpha \text{ odd}, \\ D_\alpha \cos(C_\alpha t), & \alpha \text{ even}, \end{cases} \tag{12}$$

and with the coefficients C_α and D_α given by

$$C_\alpha = \begin{cases} \frac{2\pi}{T} + \omega, & \alpha = 1, 2, \\ \frac{2\pi}{T} - \omega, & \alpha = 3, 4, \\ \omega, & \alpha = 5, 6, \end{cases} \tag{13}$$

$$D_\alpha = \begin{cases} -\frac{E_0}{4\omega}, & \alpha = 1, 2, \\ +\frac{E_0}{4\omega}, & \alpha = 3, 4, \\ +\frac{E_0}{2\omega}, & \alpha = 5, 6. \end{cases} \tag{14}$$

Furthermore, the radial functions $g_{\alpha,l}$ are expressed in terms of spherical Bessel functions j_l as

$$g_{\alpha,l}(r) = \begin{cases} j_l\left(\frac{C_\alpha}{c} r\right), & \alpha + l \text{ even}, \\ 0, & \alpha + l \text{ odd}. \end{cases} \tag{15}$$

With this we have arrived at a spherical representation of the vector potential that may be accompanied by any Hamiltonian expressed in spherical coordinates.

B. Dirac equation

In the fully relativistic formulation of the laser-matter interaction, we make use of the Dirac Hamiltonian in Eq. (3). To approach an expression of this Hamiltonian in spherical coordinates and discretize it for numerical simulations, it is convenient to express the time-dependent and time-independent parts of the Hamiltonian separately, i.e., writing

$$H = H^0 + H^I, \tag{16}$$

with

$$H^0 = \beta mc^2 + I_4 V(r) + c \sum_{i=1}^{3} \alpha_i p_i \tag{17}$$

and

$$H^I = c \sum_{i=1}^{3} \alpha_i e A_i(\boldsymbol{r}, t). \tag{18}$$

As is well known to be the case, the Dirac equation in spherical coordinates is separable into radial and angular components, with eigenstates in the angular part represented as spherical bispinors, $X_{\kappa,\mu}$. What remains then is the radial Dirac Hamiltonian,

$$H_r = \begin{pmatrix} V + mc^2 & \hbar c\left(\frac{\kappa}{r} - \frac{d}{dr}\right) \\ \hbar c\left(\frac{\kappa}{r} + \frac{d}{dr}\right) & V - mc^2 \end{pmatrix}, \tag{19}$$

where the relativistic quantum number of angular momentum κ enters as an eigenvalue of the operator K [47]:

$$K = -(\boldsymbol{\sigma} \cdot \boldsymbol{l} + I_2 \hbar). \tag{20}$$

The nature of the problem demands numerical solution, requiring a discretization scheme to be implemented, which we choose to perform along the radial axis. We represent our solutions of the time-dependent Dirac equation in a product basis of radial basis functions $P_{k,\kappa}(r)$, $Q_{k,\kappa}(r)$ and spherical bispinors $X_{\kappa,\mu}$ as

$$\Psi(\boldsymbol{r}, t) = \sum_{k,\kappa,\mu} c_{k,\kappa,\mu}(t) \psi_{k,\kappa,\mu}(\boldsymbol{r}), \tag{21}$$

with

$$\psi_{k,\kappa,\mu}(\boldsymbol{r}) = \frac{1}{r} \begin{pmatrix} P_{k,\kappa}(r) X_{\kappa,\mu}(\hat{\boldsymbol{r}}) \\ iQ_{k,\kappa}(r) X_{-\kappa,\mu}(\hat{\boldsymbol{r}}) \end{pmatrix}, \tag{22}$$

where the spherical bispinors are eigenstates of K, given by

$$X_{\kappa,\mu}(\hat{\boldsymbol{r}}) = \begin{pmatrix} C_{\mu-\frac{1}{2},\frac{1}{2},\mu}^{l_\kappa,\frac{1}{2},j} Y_{l_\kappa,\mu-\frac{1}{2}}(\hat{\boldsymbol{r}}) \\ C_{\mu+\frac{1}{2},-\frac{1}{2},\mu}^{l_\kappa,\frac{1}{2},j} Y_{l_\kappa,\mu+\frac{1}{2}}(\hat{\boldsymbol{r}}) \end{pmatrix}. \tag{23}$$

Here $C_{d,e,f}^{a,b,c}$ are the Clebsch-Gordan coefficients, $Y_{l,m}$ are spherical harmonics, and κ, μ are the relativistic angular quantum number and total magnetic angular momentum quantum number of the system, respectively. Furthermore, j is the total angular momentum quantum number and relates to κ by $j = |\kappa| - \frac{1}{2}$ and l_κ relates κ to the l quantum number by $l_\kappa = |\kappa + \frac{1}{2}| - \frac{1}{2}$.

For the radial functions $P_{k,\kappa}$, $Q_{k,\kappa}$ we use a B-spline discretization approach over evenly spaced knots [48]. However, the appearance of spurious states in discretizations of the Dirac equation necessitates the use of a dual kinetic balance [49], leading to a basis expressed as

$$
\begin{pmatrix} P_{k,\kappa} \\ iQ_{k,\kappa} \end{pmatrix} = \begin{cases} \begin{pmatrix} u_k \\ \frac{i\hbar}{2mc}\left(\frac{d}{dr} + \frac{\kappa}{r}\right)u_k \end{pmatrix}, & k \leqslant N, \\[2em] \begin{pmatrix} \frac{\hbar}{2mc}\left(\frac{d}{dr} - \frac{\kappa}{r}\right)u_{k-N} \\ iu_{k-N} \end{pmatrix}, & N < k \leqslant 2N. \end{cases}
$$

(24)

Here, we have N B-splines, with $u_k(r)$ as the kth B-spline defined over our knot interval. As the $\begin{pmatrix} P_{k,\kappa}(r) \\ iQ_{k,\kappa}(r) \end{pmatrix}$ doublet has two components, we need in total $2N$ basis functions, with basis functions of $k \leqslant N$ having large P components and basis functions of $N < k \leqslant 2N$ having large Q components.

B-splines come with the disadvantage of not being orthogonal, but in return have the advantageous property of compact support and the ability to be easily integrated numerically. As the basis is not orthogonal, we need an overlap matrix $\boldsymbol{S}$. Its matrix elements are given by

$$
\begin{aligned} S_{k,\kappa,\mu,k',\kappa',\mu'} &= \langle \psi_{k,\kappa,\mu} | \psi_{k',\kappa',\mu'} \rangle \\ &= \delta_{\kappa',\kappa}\delta_{\mu',\mu}\langle \psi_{k,\kappa,\mu} | \psi_{k',\kappa,\mu} \rangle, \end{aligned}
$$

(25)

where the orthonormality of the spherical spinors has been exploited. As will be the case with all matrices expressed in this basis, they become very sparse, taking on a block structure in which each block consists of a $2N \times 2N$ sparse matrix with $N \times N$ sub-blocks that are all band matrices, with bandwidths determined by the order of the B-splines.

The time-independent part of the Hamiltonian is projected into our basis, with matrix elements given by

$$
H_{k,\kappa,\mu,k',\kappa',\mu'}^0 = \langle \psi_{k,\kappa,\mu} | H^0 | \psi_{k',\kappa',\mu'} \rangle.
$$

(26)

This expression may be reformulated in terms of the radial Hamiltonian as

$$
\begin{aligned} H_{k,\kappa,\mu,k',\kappa',\mu'}^0 = {}& \delta_{\kappa',\kappa}\delta_{\mu',\mu}\int_0^\infty \begin{pmatrix} P_{k,\kappa}(r) \\ iQ_{k,\kappa}(r) \end{pmatrix}^\dagger \\ & \times \begin{pmatrix} V + mc^2 & \hbar c\left(\frac{\kappa}{r} - \frac{d}{dr}\right) \\ \hbar c\left(\frac{\kappa}{r} + \frac{d}{dr}\right) & V - mc^2 \end{pmatrix} \\ & \times \begin{pmatrix} P_{k,\kappa}(r) \\ iQ_{k,\kappa}(r) \end{pmatrix} dr, \end{aligned}
$$

(27)

where again the orthogonality of the spherical spinors is expressed using the Kronecker delta function δ_{ij}.

Hence, as is the case for both the $\boldsymbol{H}^0$ and $\boldsymbol{S}$ matrices, the $2N \times 2N$ blocks all lie along the main diagonal due to the

orthogonality of the basis bispinors. At this point it bears mentioning a useful feature of the block structure of the matrix $\boldsymbol{H}^0$, which is also present in $\boldsymbol{S}$. Due to the form of $\boldsymbol{H}^0$, blocks are identical when κ is the same, independently of μ. We label these repeating blocks as $\boldsymbol{H}_\kappa^0$. As μ takes half-integer values bounded by $-|\kappa| < \mu < |\kappa|$, this by itself presents a large saving of memory when the maximum allowed value of κ, $\kappa_{\max}$ grows large, requiring only a $\kappa_{\max}$-linear increase in memory, as opposed to a quadratic increase. However, there are further regularities to exploit. Note that, in both Eqs. (19) and (24), κ appears only in linear terms. Henceforth, we define

$$
\begin{aligned} \begin{pmatrix} P_{k,\kappa}(r) \\ iQ_{k,\kappa}(r) \end{pmatrix} &= R_k^0(r) + \kappa R_k^\kappa(r), \\[1em] R_k^0(r) &= \begin{pmatrix} P_{k,0}(r) \\ iQ_{k,0}(r) \end{pmatrix}, \\[1em] R_k^\kappa(r) &= \begin{pmatrix} P_{k,1}(r) \\ iQ_{k,1}(r) \end{pmatrix} - \begin{pmatrix} P_{k,0}(r) \\ iQ_{k,0}(r) \end{pmatrix}, \\[1em] H_r &= H_r^0 + \kappa H_r^\kappa, \\[1em] H_r^0 &= \begin{pmatrix} V + mc^2 & -\hbar c\frac{d}{dr} \\ \hbar c\frac{d}{dr} & V - mc^2 \end{pmatrix}, \\[1em] H_r^\kappa &= \begin{pmatrix} 0 & \frac{\hbar c}{r} \\ \frac{\hbar c}{r} & 0 \end{pmatrix}. \end{aligned}
$$

(28)

Now, we see that the matrix elements may be expressed as

$$
H_{k,\kappa,\mu,k'}^0 = \left\langle \frac{1}{r}\left(R_k^0 + \kappa R_k^\kappa\right)\middle| H_r^0 + \kappa H_r^\kappa \middle| \frac{1}{r}\left(R_{k'}^0 + \kappa R_{k'}^\kappa\right) \right\rangle.
$$

Expanding and collecting terms of equal order in κ, we then define

$$
\begin{aligned} h_{k,k'}^0 &= \langle R_k^0 | H_r^0 | R_{k'}^0 \rangle, \\ h_{k,k'}^1 &= \langle R_k^\kappa | H_r^0 | R_{k'}^0 \rangle + \langle R_k^0 | H_r^\kappa | R_{k'}^0 \rangle + \langle R_k^0 | H_r^0 | R_{k'}^\kappa \rangle, \\ h_{k,k'}^2 &= \langle R_k^\kappa | H_r^0 | R_{k'}^\kappa \rangle + \langle R_k^0 | H_r^\kappa | R_{k'}^\kappa \rangle + \langle R_k^\kappa | H_r^\kappa | R_{k'}^0 \rangle, \\ h_{k,k'}^3 &= \langle R_k^\kappa | H_r^\kappa | R_{k'}^\kappa \rangle. \end{aligned}
$$

We give the matrix elements of the four submatrices $\boldsymbol{h}^0, \ldots, \boldsymbol{h}^3$, from which we may retrieve any of the matrix blocks $\boldsymbol{H}_\kappa^0$ by

$$
\boldsymbol{H}_\kappa^0 = \boldsymbol{h}^0 + \kappa\boldsymbol{h}^1 + \kappa^2\boldsymbol{h}^2 + \kappa^3\boldsymbol{h}^3.
$$

(29)

In this way, we move from needing to store $\kappa_{\max}$ blocks of $\boldsymbol{H}^0$, where $\kappa_{\max}$ refers to the maximum value of κ (truncation) used in the expansion of the wave function in Eq. (21), to storing only the four submatrices in Eq. (29). Given that κ takes both positive and negative values, this is efficient for any $\kappa_{\max} > 2$. As the blocks of the $\boldsymbol{S}$ matrix also exhibit κ dependency due to the basis functions, we do a similar partition scheme there.

The interaction matrix is by far the most demanding part of the Hamiltonian, containing all off-diagonal blocks. Expressed in the product basis as above, our starting point

becomes

$$
\begin{aligned}
&H^I_{k,\kappa,\mu,k',\kappa',\mu'}(t) \\
&= i\left\langle X_{-\kappa,\mu}\frac{iQ_{k,\kappa}(r)}{r}\left|\sum_{i=1}^3\sigma_i A_i(\boldsymbol{r},t)\right|\frac{P_{k',\kappa'}(r)}{r}X_{\kappa',\mu'}\right\rangle \\
&\quad - i\left\langle X_{\kappa,\mu}\frac{P_{k,\kappa}(r)}{r}\left|\sum_{i=1}^3\sigma_i A_i(\boldsymbol{r},t)\right|\frac{iQ_{k',\kappa'}(r)}{r}X_{-\kappa',\mu'}\right\rangle,
\end{aligned}
\tag{30}
$$

where again the σ_i's refer to the Pauli matrices. Immediately, this introduces dependency on the particular form we have chosen for $A(\boldsymbol{r},t)$, as the polarization vector $\hat{\boldsymbol{u}}_p$ determines which Pauli matrices enter into the calculation. This in turn affects our selection rules, as the action of the Pauli matrices on the spherical spinors determines which κ, κ', μ, μ' combinations yield nonzero contributions. In addition, we have for the nondipole potential Eq. (11) a triple product between a spherical harmonic and the spherical bispinors for each term in the Bessel function expansion of the potential. This in turn is influenced by our choice of the wave vector $\hat{\boldsymbol{k}}$, as the factor of $Y_{lm}(\hat{\boldsymbol{k}})$ can be made to vanish for particular l, m through this choice. In particular, $Y_{lm}(\hat{\boldsymbol{z}}) = 0\ \forall\ m \neq 0$ makes a strong case for $\hat{\boldsymbol{k}} = \hat{\boldsymbol{z}}$, which is used here. Then, for simplicity, we choose our polarization direction as $\hat{\boldsymbol{u}}_p = \hat{\boldsymbol{x}}$. With these choices, and inserting the expansion form of the potential, we obtain

$$
\begin{aligned}
&H^I_{k,\kappa,\mu,k',\kappa',\mu'}(t) \\
&= i\sum_{\alpha=1}^6 f_\alpha(t)\sum_{l=0}^\infty Y_{l0}(\hat{\boldsymbol{z}}) \\
&\quad \times \left[\left\langle X_{-\kappa,\mu}\frac{Q_{k,\kappa}(r)}{r}\left|\sigma_x g_{\alpha,l}(r)Y_{l0}(\hat{\boldsymbol{r}})\right|\frac{P_{k',\kappa'}(r)}{r}X_{\kappa',\mu'}\right\rangle \right. \\
&\quad \left. - \left\langle X_{\kappa,\mu}\frac{P_{k,\kappa}(r)}{r}\left|\sigma_x g_{\alpha,l}(r)Y_{l0}(\hat{\boldsymbol{r}})\right|\frac{Q_{k',\kappa'}(r)}{r}X_{-\kappa',\mu'}\right\rangle\right].
\end{aligned}
\tag{31}
$$

An immediate computational benefit is now apparent: if the α terms of $\boldsymbol{H}^I$ are stored separately, we do not need to update all matrix elements at every time step. As with the preceding matrices we will not only separate $\boldsymbol{H}^I$ in terms of α, however. Recalling Eq. (28), we perform a similar substitution by

$$
\begin{aligned}
P_{k,\kappa} &\to P_{k,0} + \kappa(P_{k,1} - P_{k,0}), \\
Q_{k,\kappa} &\to Q_{k,0} + \kappa(Q_{k,1} - Q_{k,0}).
\end{aligned}
\tag{32}
$$

Usefully, there is no explicit dependency on κ in H_I in Eq. (18), i.e., κ only occurs in the definition of the dual kinetic basis functions and so matrix elements do not go to third order in κ. Instead, as we no longer have the $\delta_{\kappa,\kappa'}\delta_{\mu,\mu'}$ factor, the off-diagonal matrix blocks representing the laser-matter

interaction are given by

$$
\begin{aligned}
&\boldsymbol{H}^I_{\kappa,\mu,\kappa',\mu'}(t) \\
&= i\sum_{\alpha=1}^6 f_\alpha(t)\sum_{l=0}^{l_{\max}}H^\theta_{l,\kappa,\mu,\kappa',\mu'}\big[\boldsymbol{g}^0_{\alpha,l}+\kappa'\boldsymbol{g}^1_{\alpha,l}+\kappa\boldsymbol{g}^2_{\alpha,l}+\kappa'\kappa\boldsymbol{g}^3_{\alpha,l}\big] \\
&\quad - \big[H^\theta_{l,\kappa,\mu,\kappa',\mu'}\big]^\dagger\big[\boldsymbol{g}^0_{\alpha,l}+\kappa\boldsymbol{g}^1_{\alpha,l}+\kappa'\boldsymbol{g}^2_{\alpha,l}+\kappa'\kappa\boldsymbol{g}^3_{\alpha,l}\big]^\dagger,
\end{aligned}
\tag{33}
$$

where the matrix elements of $\boldsymbol{g}^0_{\alpha,l}\ldots\boldsymbol{g}^3_{\alpha,l}$ and the angular coupling coefficient matrices $\boldsymbol{H}^\theta_l$ are given by

$$
\begin{aligned}
g^0_{\alpha,l,k,k'} &= \int_0^{r_{\max}}Q_{k,0}(r)g_{\alpha,l}(r)dr\,P_{k',0}(r)dr, \\
g^1_{\alpha,l,k,k'} &= \int_0^{r_{\max}}Q_{k,1}(r)g_{\alpha,l}(r)dr\,P_{k',0}(r)dr, \\
g^2_{\alpha,l,k,k'} &= \int_0^{r_{\max}}Q_{k,0}(r)g_{\alpha,l}(r)dr\,P_{k',1}(r)dr, \\
g^3_{\alpha,l,k,k'} &= \int_0^{r_{\max}}Q_{k,1}(r)g_{\alpha,l}(r)dr\,P_{k',1}(r)dr, \\
H^\theta_{l,\kappa,\mu,\kappa',\mu'} &= \langle X_{-\kappa,\mu}|\sigma_x Y_{l0}(\hat{\boldsymbol{r}})|X_{\kappa',\mu'}\rangle.
\end{aligned}
\tag{34}
$$

In this way, we have reduced the memory demands of the interaction Hamiltonian to the storage of four $2N \times 2N$ submatrices per l, α combination. Note as well that, as stated in Eq. (15), $g_{\alpha,l}$ is zero for odd $\alpha + l$. Consequently, half of all $\boldsymbol{g}^0_{\alpha,l}\ldots\boldsymbol{g}^3_{\alpha,l}$ vanish and we only need to store $3 \times 4 = 12$ submatrices for each value of l that we wish to include in our simulations. However, as storage order may impact performance of matrix-multiplication libraries, as it does in the Eigen3 library [50] used in the simulation code for this work, the adjoints of the submatrices also need to be stored. Nevertheless, as each $\boldsymbol{H}^\theta_l$ has a large number of nonzero components, the memory savings easily justify this storage scheme.

Another advantage of the above-described separation scheme that is exploited in the simulation code is the ability to skip redundant calculations during evaluation of the matrix-vector product. For every $2N$-coefficient segment of the input wave vector, we perform multiplication by $\boldsymbol{g}^0_{\alpha,l}\ldots\boldsymbol{g}^3_{\alpha,l}$ only once for each submatrix relevant to it, as determined by the sparsity structure of $\boldsymbol{H}^\theta_l$. Then, the necessary linear combinations for the evaluation of our output wave vector are carried out on the segments, which is a significantly cheaper operation than linear combination of sparse matrices.

When the dipole approximation is used, the matrix elements are much simpler to calculate: in Eq. (31), we substitute $g_{\alpha,l(r)} = 1$ for $\alpha = 1$, $l = 0$, zero otherwise, and substitute $f_\alpha(t)$ with Eq. (10). In this way, all submatrices corresponding to $l \geqslant 1$ or $\alpha \geqslant 1$ vanish and only $\boldsymbol{H}^\theta_0$ is needed out of the angular coupling coefficient matrices.

C. Time propagation

The standard Crank-Nicholson propagator is used to solve for the time evolution of the system,

$$\Psi(t + \Delta t) = \left(S + i\frac{\hbar\Delta t}{2}H(t)\right)^{-1}\left(S - i\frac{\hbar\Delta t}{2}H(t)\right)\Psi(t), \tag{35}$$

where S is the overlap matrix of the basis, made necessary by the nonorthogonality of the B-splines used for the radial component of the basis, and $H = H^0 + H^I$ is the matrix representation of the total time-dependent Hamiltonian (16) in the chosen basis. We make use of the Eigen library's implementation of the iterative linear solver BiCGSTAB [51] to solve the inverse part of the propagator. By only requiring matrix-vector products to function, BiCGSTAB is well suited to this situation where keeping the full matrix in memory is infeasible. As the condition number of the matrix H is very large, a preconditioner based on ILU factorization of $S + i\frac{\hbar\Delta t}{2}H^0$ is applied to accelerate convergence. A useful feature of ILU factorization applied to this matrix is that the block structure is retained, allowing the factorization to be performed on the individual κ blocks $(S + i\frac{\hbar\Delta t}{2}H^0)_\kappa$ rather than the entire matrix. Unfortunately, ILU factorization does not allow for further separation schemes as discussed in Sec. II B and so we must store each ILU-factorized block of the preconditioner, one for each κ.

The length of time steps is the primary tunable parameter of the time evolution equation and its impact on simulation time is important to understand. As with any time integral approximation, the time steps first need to be sufficiently small for the approximation to hold. A second upper bound is imposed by the linear solver step, in which the number of iterations depends on the step size. When the step size is large, the number of iterations needed for the solver to converge increases, exacerbated by the intensity parameter E_0. As E_0 increases, smaller time steps are needed to avoid slowing the simulation to a halt with increasing convergence steps. In the scenarios considered here, time step counts in the range of 8000–16000 were typically necessary to achieve satisfactory convergence. In this range, the time cost of additional time steps dominates over the savings of reduced solver iterations.

III. RESULTS AND DISCUSSION

Prior to the interaction with the laser field, we prepare our quantum system in the hydrogenic ground state, as obtained by diagonalizing the radial Hamiltonian (19). The hydrogen $1s$ electron is then exposed to a 1.36 keV ($\omega = 50$ a.u.) laser pulse of 15-cycle duration and with varying intensities. The fully nondipole relativistic simulations with the TDDE were then ran using the Hamiltonian (3), with the potential (11). The simulation made use of a basis of $N = 250$ dual kinetic balance-enhanced B-splines for the radial component across an evenly distributed knot interval $0 \leqslant r \leqslant 30$ a.u. Varying the radial domain, as well as increasing the maximum achievable energy of the photoelectron, i.e., the number of B-spline functions, it was found that this choice for the parameters was sufficient. With our choice of polarization and propagation directions for the laser field, it is only the dipole component

of the field that couples states of different μ quantum numbers, and it was found that $|\mu| \leqslant 10$ was enough to obtain accurate results for electric-field strengths $E_0 \leqslant 600$ a.u. Likewise, for the nonrelativistic and semirelativistic nondipole calculations with the TDSE, convergence was achieved with the magnetic quantum number $|m| \leqslant 10$. Furthermore, the choice $|\kappa| \leqslant 30$ was found to be sufficient for the relativistic angular momentum quantum number, in order to achieve adequate convergence in the beyond-dipole TDDE calculations. A comprehensive convergence rate analysis for $E_0 = 400$ a.u., simply increasing the value of κ to 30 and $|\mu|$ to 16, only displayed minor fluctuations in the numerical results. Larger values of κ, $|\mu|$, and/or E_0 were not considered due to the computational demands of the nondipole Dirac simulations. When it comes to the corresponding calculations with the TDSE, however, we were allowed to push the value of the (nonrelativistic) angular momentum quantum number l up to 34 and $|m| \leqslant 30$, without finding any noticeable changes to the results for all the laser intensities considered here.

Finally, it should be noted that all the calculations in the dipole approximation, and both for the TDDE and the TDSE cases, respectively, were executed in a much larger radial domain, i.e., $0 \leqslant r \leqslant 100$ a.u., and with a high number of B-spline basis functions ($N = 1400$) allowing for large energies of the photoelectron. Yet, the obtained values for the relevant observables were all found to be in accordance with the results achieved in the smaller basis environment.

Once we had retrieved a given simulation result for the final wave function Ψ_t at the end of the laser pulse, the differential photoelectron energy spectrum was retrieved by means of projection onto the energy eigenstates $\Psi_{i,\kappa,\mu}$ (normalized on the energy scale), as obtained by solving the corresponding eigenvalue equation for the time-independent Hamiltonian H^0 in the discrete basis set, and with the index i referring to the ith (positive) eigenvalue. We then used the approximate three-point formula

$$\frac{dP}{dE_i} \approx \sum_{\kappa,\mu} \frac{|\langle \Psi_t | \Psi_{i,\kappa,\mu}\rangle|^2}{(E_{i+1,\kappa,\mu} - E_{i-1,\kappa,\mu})/2} \tag{36}$$

to estimate the value of the observable. As we operate with a finite set of eigenstates, and the energy eigenvalues for different κ, μ do not necessarily match, cubic spline interpolation was performed before the summation such that a smooth distribution could be generated. For the TDSE case, the summation over κ, μ in Eq. (36) is substituted by a summation over the ordinary angular momentum quantum numbers l, m instead.

In order to get a quantitative measure for the size of the relativistic (and/or nondipole) shifts in the location of the multiphoton resonances (cf. Fig. 1), we aimed at evaluating the energy separation between the positions of the first and second resonances in the calculated spectra. This is achieved in the following way: first, the wave functions corresponding to the net absorption of one and two photons from the field are extracted from the total wave packet, i.e., the parts of the final wave function representing the electron continuum energies in the intervals $25 < E < 75$ a.u. and $75 < E < 125$ a.u., respectively. Next, the two collected wave functions are renormalized over their respective energy domains and the
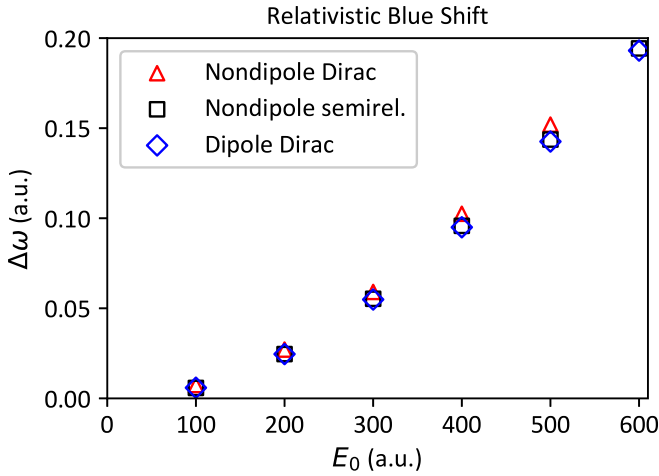
FIG. 2. Relativistic versus nonrelativistic shift in the effective frequency $\Delta\omega(A, B)$ (given in atomic units a.u.), as obtained by Eq. (37), and plotted as a function of the peak electric-field strength of the input laser field, for a 15-cycle laser pulse with $\omega = 50$ a.u. (Red triangles) Nondipole relativistic calculations with the TDDE (distribution A) versus nondipole nonrelativistic calculations with the TDSE (distribution B). (Black squares) Nondipole semirelativistic calculations with the Hamiltonian (8) (distribution A) versus nondipole nonrelativistic calculations with the Hamiltonian (2) (distribution B). (Blue diamonds) Dipole relativistic calculations with the TDDE (distribution A) versus dipole nonrelativistic calculations with the TDSE (distribution B). Main finding: the relativistic spectra are blueshifted with respect to the corresponding nonrelativistic ones.

expectation value of the energy is computed on each subinterval. The two expectation values, which are denoted by $\langle E_1 \rangle$ and $\langle E_2 \rangle$, are then used to define the position of the one- and two-photon resonances. Given an energy spectrum distribution resulting from a simulation, the measured energy separation $\Delta E = \langle E_2 \rangle - \langle E_1 \rangle$, which in turn could be translated into an effective laser frequency $\omega_{\text{eff}} = \Delta E/\hbar$, is chosen as our primary observable. Finally, the relative frequency shift between two obtained distributions A and B, where A and B could for example refer to a relativistic and nonrelativistic calculation, respectively, is defined by

$$\Delta\omega(A, B) = \omega_{\text{eff}}(A) - \omega_{\text{eff}}(B). \quad (37)$$

Note that this frequency shift may become both positive and negative valued depending on the two energy distributions involved. For positive values, we simple say that the spectrum A is blueshifted with respect to B, whereas for negative values, spectrum A is said to be redshifted with respect to B.

Figure 2 shows the shift in the effective frequency as calculated from the one- and two-photon resonance peaks, obtained by comparing the relativistic spectrum (chosen as distribution A) with the corresponding nonrelativistic one (chosen as distribution B). The relativistic shifts $\Delta\omega$ are plotted as a function of the peak electric-field strength E_0. The data points are retrieved as per Eq. (37) by comparisons of simulations ran in relativistic versus nonrelativistic environments, beginning with a comparison of full nondipole runs performed in the Dirac equation versus the Schrödinger equation (triangles, red). The second considered case is that of the semirelativistic
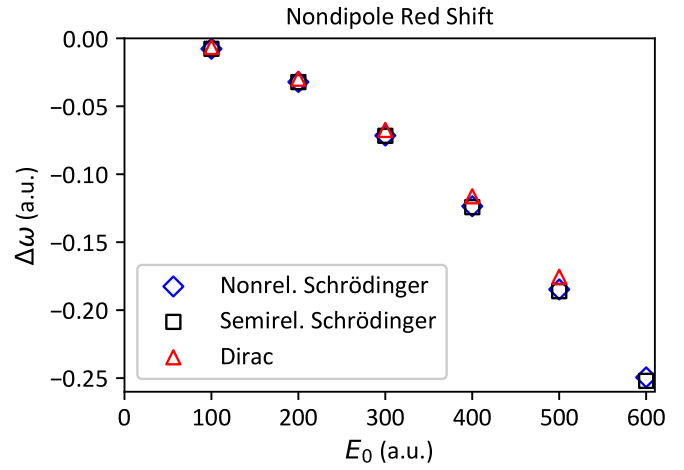

FIG. 3. Same as Fig. 2, but nondipole versus dipole approximation shift in the effective frequency $\Delta\omega(A, B)$ (given in atomic units a.u.), as obtained by Eq. (37) when comparing simulations ran with the nondipole laser field defined in Eq. (9) to those ran with the corresponding dipole field in Eq. (10). (Red triangles) Nondipole relativistic calculations with the TDDE (distribution A) versus dipole relativistic calculations with the TDDE (distribution B). (Black squares) Nondipole semirelativistic calculations with the Hamiltonian (8) versus dipole semirelativistic calculations (distribution B). (Blue diamonds) Nondipole nonrelativistic calculations with the Hamiltonian (2) (distribution A) versus dipole nonrelativistic calculations with the TDSE (distribution B). Main finding: the nondipole spectra are redshifted with respect to the corresponding dipole ones.

versus the nonrelativistic one (squares, black), i.e., comparing results obtained with Eqs. (8) and (2), respectively, still retaining the full spatial dependence of the nondipole field. Finally, the third data set (diamonds, blue) shows the Dirac-Schrödinger shift calculated in the dipole approximation. As can be seen from the figure, the three different scenarios produce near identical results, effectively yielding a relativistic blueshift of the spectrum, with $\Delta\omega$ increasing as a function of E_0 in the same manner for all three situations. This close agreement suggests that the beyond-dipole component of the laser field is redundant from the point of view of the blueshift, and that magnetic-field effects as well as relativistic structure and spin-related effects are of minor importance for the relativistic shifting of the spectrum.

Yet, the magnetic field throws a spanner into the works, in that the combined effect of the electric and magnetic fields, i.e., the radiation pressure of the intense laser light, requires further attention. This nondipole effect enters as a consequence of including the full spatial dependence of our external vector potential [cf. Eq. (11)] in the Hamiltonian (2), and the so resulting (red) shift is primarily of nonrelativistic origin. Figure 3 shows the calculated shift $\Delta\omega$ as a function of E_0, as obtained by comparing nondipole (chosen as distribution A) and dipole (chosen as distribution B) simulation data. Nondipole (A) versus dipole (B) results for the Dirac (triangles, red), the semirelativistic Schrödinger (squares, black), and the nonrelativistic Schrödinger equation (diamonds, blue) are all shown for comparison. Again we see that the three cases chosen agree to a high degree, simply expressing the
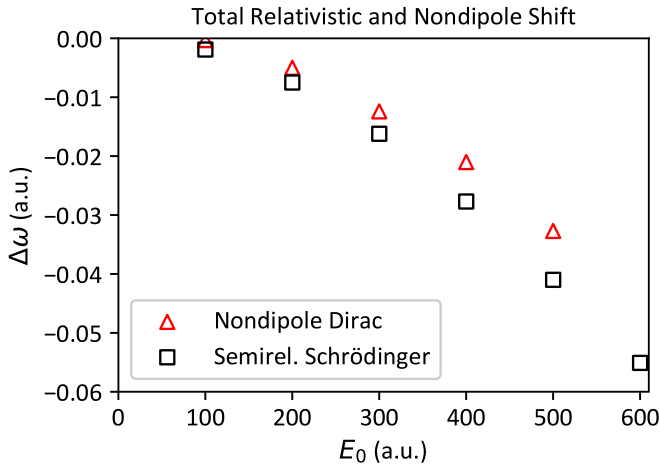
FIG. 4. Nondipole relativistic versus dipole nonrelativistic shift in the effective frequency $\Delta\omega(A, B)$ (given in atomic units a.u.), as obtained by Eq. (37), and plotted as a function of the peak electric-field strength of the input laser field, for a 15-cycle laser pulse with $\omega = 50$ a.u. (Red triangles) Nondipole relativistic calculations with the TDDE (distribution A) versus dipole nonrelativistic calculations with the TDSE (distribution B). (Black squares) Nondipole semirelativistic calculations with the Hamiltonian (8) (distribution A) versus dipole nonrelativistic calculations with the TDSE (distribution B). Main finding: the total relativistic nondipole spectra are slightly redshifted with respect to the corresponding nonrelativistic dipole ones.

same increase in the shift magnitude as a function of E_0. However, in clear contrast to the previously reported relativistic blueshift, the shift now becomes negative, i.e., nondipole effects are responsible for a corresponding redshift of the energy spectrum. Moreover, the nondipole redshift turns out to be of the same magnitude as the relativistic blueshift, differing primarily by being aligned in the opposite direction, which is concerning though, as it now appears to be possible that in a real life scenario there will be no remaining shift to be observed in the experiment or that the measured shift will be only very small. The relative role of the relativistic blueshift with respect to the nondipole redshift was also recently addressed within the context of a simpler model accounting for beyond-dipole and relativistic effects to lowest order [9,40], yet similar results were obtained for the shifts further supporting the finding of their mutual near cancellation.

This leads into our next point of comparison, i.e., that between relativistic nondipole and nonrelativistic dipole calculations, respectively. Figure 4 shows the so computed shifts obtained from comparing nonrelativistic (Schrödinger equation), dipole data with the relativistic nondipole ones, using both the semirelativistic (squares, black) and the fully relativistic (triangles, red) approaches, respectively. Here the relativistic nondipole results are taken as distribution A in Eq. (37), whereas the nonrelativistic dipole results are chosen as distribution B. As can be read from the figure, the effective shift, when accounting for both the relativistic blueshift and the nondipole redshift, turns out to be negative (redshift), but it is noticeably smaller in magnitude than either of the preceding shifts (note the smaller range of the y axis shown in the figure). This was expected though given what we already learned from

Figs. 2 and 3, with the blue- and redshifts having come close to canceling.

Comparing the results obtained with the semirelativistic Schrödinger and Dirac equations, respectively, in Fig. 4, we find that there are some remaining discrepancies in the calculated values for the redshift, i.e., the magnitude of the shift computed with the nondipole Dirac equation is somewhat smaller in numeric value than the corresponding semirelativistic one. There are several possible reasons for this, with the first among them being the clear possibility of insufficient convergence in the nondipole Dirac simulations due to the time steps being too large. Reducing the time step size even further resulted in better agreement with the semirelativistic calculations, but still the convergence rate was slow, merely demonstrating the fact that the time-dependent Dirac equation is notoriously hard to solve numerically. This is due to the existence of the negative energy continuum and the large contribution from the electron's rest-mass energy term in the Dirac Hamiltonian. Other possible candidates for explaining the disagreement between the two models are the interaction of the electron's spin with the magnetic field and/or spin-orbit effects, as spin-related effects were not considered in the semirelativistic approach. Lastly, and most importantly, we would like to emphasize that even though some disagreements in the exact numeric values are expressed, both models agree largely upon the sign of the resulting net shift, i.e., the total energy spectrum becomes slightly redshifted when both relativistic and beyond-dipole effects are accounted for.

Keeping in mind that the primary goal of our investigation was to probe relativistic and nondipole effects in the multi-photon ionization of hydrogen as induced by intense x-ray laser pulses, then the observations made in Figs. 2–4, with the near cancellation of relativistic and nondipole shifts, are somewhat disappointing. From this, it is tempting to conclude that relativity is not really necessary in order to explain the underlying ionization dynamics. As a matter of fact, we will now demonstrate that this is indeed not the case, and that the relativistic blueshift may be recovered. To this end, we will make extensive use of the semirelativistic light-matter interaction formulations (5) and (8).

In a recent work [40], and by means of a unitary transformation applied to the system wave function, it was shown that the effect of the last (relativistic) term in Eqs. (5) and (8) effectively loses its importance and cancels exactly against a similar (nondipole) contribution contained in the $A(r, t) \cdot p$ interaction term. This suggests that there is an intimate interplay between nondipole and relativistic effects in the system and that they cannot simply be treated separately. Based on this finding, a more suitable choice for the nonrelativistic Hamiltonian would be

$$H_{\text{nonrel}} = \frac{p^2}{2m} + V + \frac{e}{m}\boldsymbol{A} \cdot \boldsymbol{p} + \frac{e^2}{2m}A^2 - \frac{e^2}{2m^3c^2}(\boldsymbol{A} \cdot \boldsymbol{p})^2,$$

(38)

where the cancellation is implicitly taken into account in the formulation. For further details on the cancellation effect the reader is referred to Ref. [40]. Please notice that the construction (38) is highly nonstandard, and we will here simply use it as a means to interpret the results. In fact, if we were to use H_{nonrel} as our ansatz for the nondipole nonrelativistic

Hamiltonian, then the consequence would have been that both the relativistic blueshifts in Fig. 2 and the nondipole redshifts in Fig. 3 would diminish, merely manifesting the cancellation effect.

Another interesting and appealing feature of the formulation (38) is that photoelectrons that are emitted along the laser polarization axis are left unaltered by the nondipole field, i.e., no (nondipole) shifts in the resonance positions with respect to the dipole counterparts are expected in this direction. As such, the main role of the propagating laser field is to exert a radiation pressure on the electron in the propagation direction, and only electrons that are emitted with a nonzero momentum component along the axis of propagation are influenced by the nondipole field. Now, turning back to the semirelativistic formulation in Eq. (5), and taking advantage of the fact that the term proportional to $\{A \cdot p, p^2\}$ can be shown to have only vanishingly small impact on the relativistic ionization dynamics, a more useful choice for the semirelativistic Hamiltonian would be

$$H_{\rm rel} = \frac{p^2}{2m} + V + \frac{e}{m}A \cdot p + \frac{e^2}{2m}A^2 - \frac{e^2}{2m^3c^2}(A \cdot p)^2$$
$$- \frac{e^3}{2m^3c^2}A^2A \cdot p - \frac{e^2}{8m^3c^2}\{A^2, p^2\}. \quad (39)$$

Notice here that we have also omitted the A^4 term as it does not contribute in lowest order. On this somewhat reduced form, the semirelativistic Hamiltonian (39) only differs from the nonrelativistic one (38) by the last two terms, both of which will shortly be shown to play the role of a (time-dependent) relativistic mass shift.

Equation (39) can be even further simplified if we only consider photoelectrons whose movement is restricted to a line that is aligned with the polarization of the driving laser field. In this limit, the dipole approximation may be reintroduced, the remaining time-dependent A_0^2 term may be omitted, and the semirelativistic light-matter interaction formulation takes the simpler form,

$$H_{\rm rel}^{\rm dipole} = \frac{p^2}{2m} + V + \frac{e}{m}A_0(t) \cdot p - \frac{e^3}{2m^3c^2}A_0^2(t)A_0(t) \cdot p$$
$$- \frac{e^2}{4m^3c^2}p^2A_0^2(t), \quad (40)$$

valid for photoelectrons that are emitted along the laser polarization axis only. Because of the aforementioned beyond-dipole cancellation effect, and for consistency, also the $(A \cdot p)^2$ term was abandoned in Eq. (40). Finally, noticing that the Hamiltonian (40) only represents the lowest-order expansion of the more general formulation [42],

$$H_{\rm rel}^{\rm dipole} = \frac{p^2}{2\mu} + V + \frac{e}{\mu}A_0(t) \cdot p, \quad (41)$$

where

$$\mu = m\left[1 + \frac{e^2}{2m^2c^2}A_0^2(t)\right] \quad (42)$$

is recognized as the (time-dependent) relativistic mass of the (free) electron in the (dipole) laser field, we will now make extensive use of the model (41) in the interpretation of our
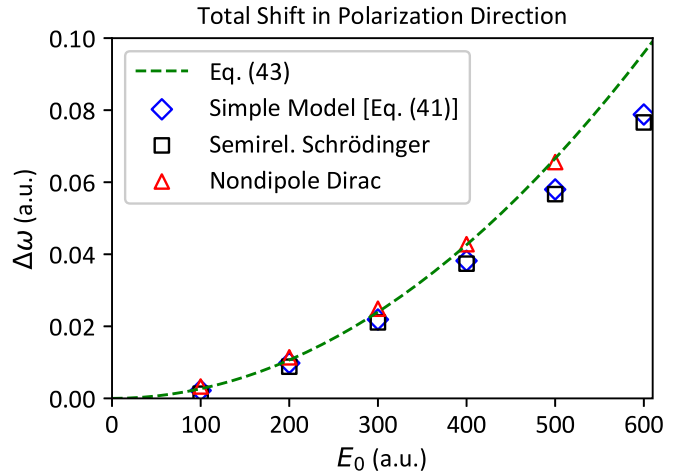

FIG. 5. Same as Fig. 4, but nondipole relativistic versus dipole nonrelativistic shift, Eq. (37), as obtained for photoelectrons that are emitted along the laser polarization axis. (Red triangles) Nondipole relativistic calculations with the TDDE (distribution A) versus dipole nonrelativistic calculations with the TDSE (distribution B). (Black squares) Nondipole semirelativistic calculations with the Hamiltonian (8) (distribution A) versus dipole nonrelativistic calculations with the TDSE (distribution B). (Blue diamonds) Calculations with the simple (relativistic) model (41) (distribution A) versus dipole nonrelativistic calculations with the TDSE (distribution B). (Green dashed line) Scaling law given by Eq. (43). Main finding: for photoelectrons that are emitted along the laser polarization direction, the relativistic spectra become blueshifted with respect to the corresponding nonrelativistic dipole ones.

results. But first we will have to establish the validity of this simple model picture.

Figure 5 shows the calculated frequency shift [cf. Eq. (37)], along the laser polarization direction, as a function of the peak electric-field strength of the input laser field, obtained from comparing relativistic data (chosen as distribution A) and nonrelativistic data (chosen as distribution B), respectively. Keeping in mind the approximations and assumptions made when deriving Eq. (41), there is a remarkably good agreement between the (fully) semirelativistic model (black squares) and the simple model (blue diamonds) in the figure. Furthermore, they both yield results compatible with the Dirac equation (red triangles). Although of smaller magnitude than in Fig. 2, the results in Fig. 5 clearly demonstrate that the relativistic blueshift is retrieved when considering photoelectrons that are emitted parallel to the polarization axis of the incident light. But even more importantly, the resulting shift may be explained physically in terms of the (time-dependent) relativistic mass increase, cf. Eq. (42), of the electron in the oscillating laser field.

Having settled the validity of the simple model and the time-dependent effective mass, we may now use these to derive an analytical formula for the relativistic energy shift. To this end, taking the laser field to be monochromatic, for simplicity, and substituting the time-dependent relativistic mass with its mean value $\bar{\mu}$ in Eqs. (41) and (42), i.e., the average value of μ over a laser period, then the (average) relativistic kinetic energy of the (free) electron oscillating in the laser

field becomes shifted by a factor $(\frac{\bar{\mu}}{m} - 1)$ with respect to its nonrelativistic counterpart. This suggests that the frequency shift $\Delta\omega$ in Eq. (37) follows the scaling law

$$\Delta\omega \simeq \left(\frac{\bar{\mu}}{m} - 1\right)\frac{\Delta E}{\hbar} \simeq \left(\frac{\bar{\mu}}{m} - 1\right)\omega = \frac{e^2 E_0^2}{4m^2\omega c^2}. \quad (43)$$

The result of Eq. (43) is plotted in Fig. 5 against the numerical data. As it turns out, the predicted shift is in excellent agreement with the calculated values, merely demonstrating the importance of the relativistic mass shift in the underlying ionization dynamics.

At this point, the attentive reader may have made the important observation that the blueshift reported in Fig. 2 is about a factor two larger than the shift found in Fig. 5. In fact, this difference can be attributed to the cancellation effect discussed previously and the resulting absence of the $(\boldsymbol{A} \cdot \boldsymbol{p})^2$ term in the final model Hamiltonian Eq. (41). As a matter of fact, if it were not for this cancellation, we could no longer have associated the remaining shift observed in Fig. 5 with the relativistic mass shift. This indicates that the part of the shift that has canceled out ultimately has no distinct physical implication, but is rather related to the choice of gauge for the representation of the light-matter interaction.

IV. CONCLUSION

Laser-induced multiphoton ionization of atomic hydrogen by some intense and short x-ray laser pulse is modeled in terms of the time-dependent Dirac and Schrödinger equations, respectively, retaining the full spatial dependence of the external electromagnetic field. The equations of motion are solved for the relevant relativistic and nonrelativistic ionization dynamics both within and beyond the electric dipole approximation. The resulting kinetic-energy spectrum of the emitted photoelectron is analyzed in some detail, and it is found that relativistic effects are generally responsible for a shifting of the spectrum to higher energies with respect to the corresponding spectrum obtained in the nonrelativistic limit. The strength of this relativistic blueshift is computed as a function of the intensity of the input laser field. Then, a semirelativistic model, including only field-induced relativistic corrections to lowest order and ignoring relativistic structure effects as well as any spin degrees of freedom, is proposed and tested against the fully relativistic calculations, and it is shown to yield results for the blueshift in good agreement with the Dirac equation.

Next, the validity of the dipole approximation is investigated in some detail, and it is found that beyond-dipole (nondipole) effects generally impose a corresponding redshift of the energy spectrum. As it turns out, the relativistic blue- and nondipole redshifts are of equal order of magnitude and the net shifts are only very small. Nonetheless, ultimately remnants of tiny redshifts are exposed in the total spectra when comparing fully relativistic, nondipole data with corresponding nonrelativistic, dipole ones. Calculations executed in the semirelativistic model provide further evidence for the existence of the resulting redshifts. Inspecting the photoelectrons that are emitted in the laser polarization direction, though, the relativistic blueshift returns, albeit somewhat smaller in magnitude than before, and it can be shown to be caused by the relativistic mass increase of the electron in the intense field.

In conclusion, we have demonstrated that in the high-energy regime of multiphoton ionization there is a net redshift in the power spectrum caused by a combination of relativistic and nondipole effects, and quantified its relation to the intensity of the incident laser pulse. The cancellation of nondipole and relativistic effects has been demonstrated and what remains has been calculated. The results raise further questions to be investigated in future works: the relative magnitudes of the nondipole and relativistic effects are both directionally dependent in nature, and so a treatment in which they are analyzed in a directionally dependent framing could provide further insight into the dynamics. Furthermore, here the analysis was outlined in the x-ray regime only and longer-wavelength light should be considered. It is worth mentioning, however, that in a previous study on strong-field ionization by xuv light [34], a corresponding redshift as caused by higher-order nondipole effects was reported.

[1] Y. I. Salamin, S. X. Hu, K. Z. Hatsagortsyan, and C. H. Keitel, Relativistic high-power laser–matter interactions, Phys. Rep. **427**, 41 (2006).

[2] A. Di Piazza, C. Müller, K. Z. Hatsagortsyan, and C. H. Keitel, Extremely high-intensity laser interactions with fundamental quantum systems, Rev. Mod. Phys. **84**, 1177 (2012).

[3] S. Selstø, E. Lindroth, and J. Bengtsson, Solution of the Dirac equation for hydrogenlike systems exposed to intense electromagnetic pulses, Phys. Rev. A **79**, 043418 (2009).

[4] H. Bauke, H. G. Hetzheim, G. R. Mocken, M. Ruf, and C. H. Keitel, Relativistic ionization characteristics of laser-driven hydrogenlike ions, Phys. Rev. A **83**, 063414 (2011).

[5] Y. V. Vanne and A. Saenz, Solution of the time-dependent Dirac equation for multiphoton ionization of highly charged hydrogenlike ions, Phys. Rev. A **85**, 033411 (2012).

[6] T. Kjellsson, S. Selstø, and E. Lindroth, Relativistic ionization dynamics for a hydrogen atom exposed to superintense XUV laser pulses, Phys. Rev. A **95**, 043403 (2017).

[7] I. A. Ivanov, Spin-flip processes and nondipole effects in above-threshold ionization of hydrogen in ultrastrong laser fields, Phys. Rev. A **96**, 013419 (2017).

[8] I. V. Ivanova, V. M. Shabaev, D. A. Telnov, and A. Saenz, Scaling relations of the time-dependent Dirac equation describing multiphoton ionization of hydrogenlike ions, Phys. Rev. A **98**, 063402 (2018).

[9] M. Førre, Breakdown of the nonrelativistic approximation in superintense laser-matter interactions, Phys. Rev. A **99**, 053410 (2019).

[10] T. K. Lindblom, M. Førre, E. Lindroth, and S. Selstø, Relativistic effects in photoionizing a circular Rydberg

state in the optical regime, Phys. Rev. A **102**, 063108 (2020).

[11] D. A. Telnov and S.-I. Chu, Relativistic ionization probabilities and photoelectron distributions of hydrogenlike ions in superstrong electromagnetic fields, Phys. Rev. A **104**, 023111 (2021).

[12] T. K. Lindblom and S. Selstø, Relativistic photoionization with elliptically polarized laser fields in the ultraviolet region, Phys. Rev. A **104**, 043102 (2021).

[13] N. J. Kylstra, R. A. Worthington, A. Patel, P. L. Knight, J. R. Vázquez de Aldana, and L. Roso, Breakdown of stabilization of atoms interacting with intense, high-frequency laser pulses, Phys. Rev. Lett. **85**, 1835 (2000).

[14] M. Førre, S. Selstø, J. P. Hansen, and L. B. Madsen, Exact nondipole Kramers-Henneberger form of the light-atom Hamiltonian: An application to atomic stabilization and photoelectron energy spectra, Phys. Rev. Lett. **95**, 043601 (2005).

[15] M. Førre, J. P. Hansen, L. Kocbach, S. Selstø, and L. B. Madsen, Nondipole ionization dynamics of atoms in superintense high-frequency attosecond pulses, Phys. Rev. Lett. **97**, 043601 (2006).

[16] M. Førre, S. Selstø, J. P. Hansen, T. K. Kjeldsen, and L. B. Madsen, Molecules in intense xuv pulses: Beyond the dipole approximation in linearly and circularly polarized fields, Phys. Rev. A **76**, 033415 (2007).

[17] H. Bachau, M. Dondera, and V. Florescu, Stimulated compton scattering in two-color ionization of hydrogen with keV electromagnetic fields, Phys. Rev. Lett. **112**, 073001 (2014).

[18] N. Haram, R. T. Sang, and I. V. Litvinyuk, Transverse electron momentum distributions in strong-field ionization: Nondipole and Coulomb focusing effects, J. Phys. B: At. Mol. Opt. Phys. **53**, 154005 (2020).

[19] M. M. Lund and L. B. Madsen, Nondipole photoelectron momentum shifts in strong-field ionization with mid-infrared laser pulses of long duration, J. Phys. B: At. Mol. Opt. Phys. **54**, 165602 (2021).

[20] L. Geng, H. Liang, K. Krajewska, L.-Y. Peng, and Q. Gong, Laser-induced electron fresnel diffraction by XUV pulses at extreme intensity, Phys. Rev. A **104**, L021102 (2021).

[21] L. B. Madsen, Nondipole effects in tunneling ionization by intense laser pulses, Phys. Rev. A **105**, 043107 (2022).

[22] M. Førre, Nondipole effects and photoelectron momentum shifts in strong-field ionization by infrared light, Phys. Rev. A **106**, 013104 (2022).

[23] O. Hemmers, R. Guillemin, E. P. Kanter, B. Krässig, D. W. Lindle, S. H. Southworth, R. Wehlitz, J. Baker, A. Hudson, M. Lotrakul, D. Rolles, W. C. Stolte, I. C. Tran, A. Wolska, S. W. Yu, M. Y. Amusia, K. T. Cheng, L. V. Chernysheva, W. R. Johnson, and S. T. Manson, Dramatic nondipole effects in low-energy photoionization: Experimental and theoretical study of Xe 5*s*, Phys. Rev. Lett. **91**, 053002 (2003).

[24] C. T. L. Smeenk, L. Arissian, B. Zhou, A. Mysyrowicz, D. M. Villeneuve, A. Staudte, and P. B. Corkum, Partitioning of the linear photon momentum in multiphoton ionization, Phys. Rev. Lett. **106**, 193002 (2011).

[25] S. Eilzer, H. Zimmermann, and U. Eichmann, Strong-field Kapitza-Dirac scattering of neutral atoms, Phys. Rev. Lett. **112**, 113001 (2014).

[26] A. Ludwig, J. Maurer, B. W. Mayer, C. R. Phillips, L. Gallmann, and U. Keller, Breakdown of the dipole

approximation in strong-field ionization, Phys. Rev. Lett. **113**, 243001 (2014).

[27] M. Ilchen, G. Hartmann, E. V. Gryzlova, A. Achner, E. Allaria, A. Beckmann, M. Braune, J. Buck, C. Callegari, R. N. Coffee, R. Cucini, M. Danailov, A. De Fanis, A. Demidovich, E. Ferrari, P. Finetti, L. Glaser, A. Knie, A. O. Lindahl, O. Plekan *et al.*, Symmetry breakdown of electron emission in extreme ultraviolet photoionization of argon, Nat. Commun. **9**, 4659 (2018).

[28] H. Zimmermann, S. Meise, A. Khujakulov, A. Magaña, A. Saenz, and U. Eichmann, Limit on excitation and stabilization of atoms in intense optical laser fields, Phys. Rev. Lett. **120**, 123202 (2018).

[29] N. Haram, I. Ivanov, H. Xu, K. T. Kim, A. Atia-tul Noor, U. S. Sainadh, R. D. Glover, D. Chetty, I. V. Litvinyuk, and R. T. Sang, Relativistic nondipole effects in strong-field atomic ionization at moderate intensities, Phys. Rev. Lett. **123**, 093201 (2019).

[30] A. Hartung, S. Eckart, S. Brennecke, J. Rist, D. Trabert, K. Fehre, M. Richter, H. Sann, S. Zeller, K. Henrichs, G. Kastirke, J. Hoehl, A. Kalinin, M. S. Schöffler, T. Jahnke, L. P. H. Schmidt, M. Lein, M. Kunitski, and R. Dörner, Magnetic fields alter strong-field ionization, Nat. Phys. **15**, 1222 (2019).

[31] B. Willenberg, J. Maurer, B. W. Mayer, and U. Keller, Subcycle time resolution of multi-photon momentum transfer in strong-field ionization, Nat. Commun. **10**, 5548 (2019).

[32] A. Hartung, S. Brennecke, K. Lin, D. Trabert, K. Fehre, J. Rist, M. S. Schöffler, T. Jahnke, L. P. H. Schmidt, M. Kunitski, M. Lein, R. Dörner, and S. Eckart, Electric nondipole effect in strong-field ionization, Phys. Rev. Lett. **126**, 053202 (2021).

[33] T. E. Moe and M. Førre, Ionization of atomic hydrogen by an intense x-ray laser pulse: An *ab initio* study of the breakdown of the dipole approximation, Phys. Rev. A **97**, 013415 (2018).

[34] M. Førre and A. S. Simonsen, Nondipole ionization dynamics in atoms induced by intense xuv laser fields, Phys. Rev. A **90**, 053411 (2014).

[35] J. W. Braun, Q. Su, and R. Grobe, Numerical approach to solve the time-dependent Dirac equation, Phys. Rev. A **59**, 604 (1999).

[36] M. S. Pindzola, S. A. Abdel-Naby, F. Robicheaux, and J. Colgan, Single photoionization of highly charged atomic ions including the full electromagnetic-field potential, Phys. Rev. A **85**, 032701 (2012).

[37] I. A. Ivanov, Relativistic calculation of the electron-momentum shift in tunneling ionization, Phys. Rev. A **91**, 043410 (2015).

[38] R. Beerwerth and H. Bauke, Krylov subspace methods for the dirac equation, Comput. Phys. Commun. **188**, 189 (2015).

[39] D. A. Telnov and S.-I. Chu, Relativistic ionization dynamics of hydrogenlike ions in strong electromagnetic fields: Generalized pseudospectral method for the time-dependent Dirac equation, Phys. Rev. A **102**, 063109 (2020).

[40] M. Førre and S. Selstø, Schrödinger formulation of the nondipole light-matter interaction consistent with relativity, Phys. Rev. A **101**, 063416 (2020).

[41] T. K. Lindblom, M. Førre, E. Lindroth, and S. Selstø, Semirelativistic Schrödinger equation for relativistic laser-matter interactions, Phys. Rev. Lett. **121**, 253202 (2018).

[42] T. K. Lindblom, M. Førre, E. Lindroth, and S. Selstø, Erratum: Semirelativistic Schrödinger equation for relativistic

laser-matter interactions [Phys. Rev. Lett. **121**, 253202 (2018)], Phys. Rev. Lett. **127**, 149902(E) (2021).

[43] T. Kjellsson, M. Førre, A. S. Simonsen, S. Selstø, and E. Lindroth, Alternative gauge for the description of the light-matter interaction in a relativistic framework, Phys. Rev. A **96**, 023426 (2017).

[44] L. Geng, H. Liang, Z.-Y. Lin, and L.-Y. Peng, Solving the time-dependent Klein-Gordon and square-root Klein-Gordon equations with Krylov-subspace methods, Phys. Rev. A **107**, 053115 (2023).

[45] H. R. Reiss, Dipole-approximation magnetic fields in strong laser beams, Phys. Rev. A **63**, 013409 (2000).

[46] H. R. Reiss, Limits on tunneling theories of strong-field ionization, Phys. Rev. Lett. **101**, 043002 (2008).

[47] I. P. Grant, *Relativistic Quantum Theory of Atoms and Molecules: Theory and Computation* (Springer, New York, NY, 2007).

[48] H. Bachau, E. Cormier, P. Decleva, J. E. Hansen, and F. Martín, Applications of *B*-splines in atomic and molecular physics, Rep. Prog. Phys. **64**, 1815 (2001).

[49] V. M. Shabaev, I. I. Tupitsyn, V. A. Yerokhin, G. Plunien, and G. Soff, Dual kinetic balance approach to basis-set expansions for the Dirac equation, Phys. Rev. Lett. **93**, 130405 (2004).

[50] G. Guennebaud *et al.*, Eigen v3, http://eigen.tuxfamily.org.

[51] H. A. van der Vorst, Bi-CGSTAB: A fast and smoothly converging variant of Bi-CG for the solution of nonsymmetric linear systems, SIAM J. Sci. Comput. **13**, 631 (1992).